A NOVEL COUPLING DISCRETIZATION METHOD FOR MODELING MULTI-PHASE HEAT EXCHANGERS

***Zhenhao Chu*[1,*]*, Daocang Che*[1]*, Zhaowang Xia*[1]

[1] Jiangsu University of Science and Technology, 212100, Jiangsu, People's Republic of China

[*] Corresponding author; E-mail: zhenhaochu@just.edu.cn

This paper presents a novel coupling discretization method for modeling multi-phase heat exchangers. In the method, the MBM (Moving Boundary Method) is adopted as the solver to solve each of the FVCVs (Finite Volume Control Volume) divided by the method of FVM (Finite Volume Method). When all FVCVs are solved, the FVCV boundary values are updated based on the relationships of FVCVs. The solving procedure is initiated when the starting values of HSF (Hot Source Fluid) and CSF (Cold Source Fluid) outlet of the heat exchanger are given by the user and terminated when these values no longer change anymore. The experimental results of a plate heat exchanger with R245fa and Therminol 66 as CSF and HSF are adopted to validate the proposed model. Simulation results of 11 operating conditions show that the maximum deviation is within ±4% compared to the measured values. The model presented in this paper is appropriate for heat exchangers under operating conditions either with or without fluid phase change, such as the evaporator and condenser in the ORC (Organic Rankine Cycle) system.

Key words*: Multi-Phase Heat Exchanger, FVM, MBM, ORC, Coupling Discretization*

1. Introduction

ORC is a currently rapid development technology and is already adopted in the recovery of diesel engines waste heat energy [1], solar energy, geothermal energy and industrial waste heat energy [2]. The typical ORC system is shown in Fig. 1, in which six major components exist in the ORC system. Where, the heat exchangers are treated as the most important components in the ORC system since their performance has a huge impact on the compactness and cost of the ORC system. Therefore, the modeling and solution of the heat exchanger are treated as the key sub-procedures to evaluate the performance, compactness and cost of the ORC system. In the heat exchanger design books, the heat exchangers are modelled by the LMTD and ε-NTU [3], with which only the external boundary parameters or the geometry parameters of the heat exchanger can be calculated. Moreover, the phase change of the fluids in the heat exchanger is neglected in these methods, thus restricting the application in the ORC system.

In order to analyze the performance of plate heat exchangers with multi-fluid, multi-stream and multi-pass configurations, Qiao [4] provided an FVM-based model to solve the problem. Patiño [5] and Chowdhury [6] proposed an FVM-based model to model the multi-phase heat exchangers.

Yohanis [7] proposed an enthalpy-based method to solve the heat transfer problem in which one or two fluids phase change happens. For the purpose of developing a general heat exchanger model applying to both super and sub-critical fluids in the heat recovery system, Zegenhagen [8] developed an FVM-based heat exchanger model to solve the problem. Vijaya [9] developed a steady state ORC system simulation tool to predict the performance of the ORC system. The method reported by Bell [10] is a fast and robust algorithm to predict the steady state performance of the heat exchanger. The experimental results of the 11 kWe prototype ORC and the off-design ORC model are presented by Lecompte [11]. In their paper, the off-design ORC model is validated by the experimental results. In the off-design ORC model, a hybrid heat exchanger model which combines the FVM and MBM is employed. Sarfraz [12] presents a detailed segment-by-segment model of a fin-tube heat exchanger that calculates the conduction between all the adjacent tube segments through the fins. Taler [13] provides a new heat exchanger model based on FVM. The gas temperature across a tube row is calculated by integral. Huang [14] compares three approximation-assisted heat exchanger models for the steady state simulation of vapor compression system. Bone [15] presents a methodology to develop accurate and computationally efficient on- and off-design models of heat exchangers that exhibit complex nonlinear behaviours. Jahn [16] describes a quasi 1-D segment by segment heat exchanger model that can be used for the design and evaluation process. Hagen [17] presents a generic counter current heat exchanger model for cycle optimization process. Chu proposes a moving-boundary and finite-volume coupling method to solve the heat exchangers whether fluid phase on both sides changes or not.

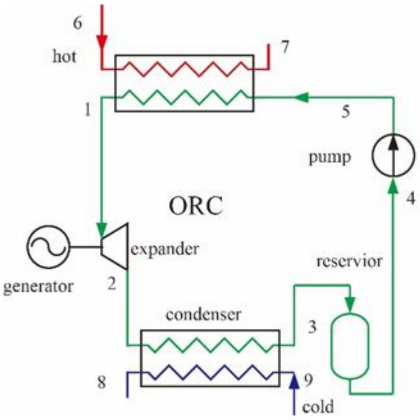

Fig. 1 Typical ORC system

In the present work, a novel coupling discretization method for modeling heat exchangers is proposed. In the method, the heat exchanger is first discretised based on FVM and then MBM is applied to each of the FVCVs divided by FVM. The phase change CV determination procedure in FVM is omitted in the proposed coupling discretization method, which decreases the complexity of the FVM. The following parts of the paper are organized as follows. Section 2 presents the details of the novel coupling discretization method for modeling heat exchangers. Section 3 describes the validation results of the model and the experimental data is presented in paper [11]. Section 4 describes a case study of an evaporator in the ORC system. Section 5 reports the conclusions of this paper.

2. Methodology

For the heat exchanger model based on the coupling discretization method, the heat exchanger is first divided into multiple CVs according to FVM and then a single CV is furthermore dealing with

MBM. For the purpose of avoiding confusion, the CVs divided by FVM are referred to as FVCV and the CVs divided by MBM are referred to as MBCV in the following parts of the paper. The flow chart of the heat exchanger model based on the coupling discretization method is shown in Fig. 2. It can be seen from Fig. 2 that four steps are needed to constitute the solver of the heat exchanger model namely the determination of the initial values of the geometry parameters of the heat exchanger, setting initial values of FVCVs which includes boundary values and heat transfer areas, solving FVCV using MBM, and updating FVCVs boundary values. The detailed description of the processes is shown in section 2.3 to 2.5. It should be pointed out that the flow chart shown in Fig. 2 is very compact and the phase change CV identification procedures are simplified in the original FVM with MBM being able to deal with phase change of the fluid in FVCV. Once all of the FVCVs are solved with MBM, the FVCVs boundary values can be updated and then the convergence of the solution can be reached. The processes 2), 3) and 4) will be repeated until the convergence criteria can be satisfied. The solving process based on the assumptions is shown below:

1. The heat transfer from the evaporator to the environment is negligible;
2. The fouling of evaporator is negligible;
3. The pressure drop of HSF and CSF flows through the heat exchanger is negligible;
4. The flow of HSF and CSF in the heat exchanger is simplified as one dimensional flow;

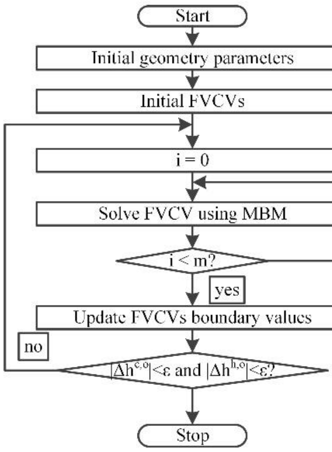

Fig. 2 Flow chart of the novel coupling discretization method for modeling heat exchangers

2.1. Constitution and relationship of the CV

The mesh of the MBM and FVM is the combination of multiple CVs, where a possible CV is shown in Fig. 3. It can be seen from Fig. 3 that the CV includes inlet, outlet and center nodes. The fluid thermophysical parameters are needed by the algorithm, such as p, T, h, s, X, stored in the nodes for the purpose of facilitating the program writing. The thermophysical parameters of the center nodes of HSF and CSF are calculated by linear interpolation of the inlet and outlet nodes, as shown in Equation (1) and (2) respectively. Similarly, the wall temperature is calculated by linear interpolation of the center temperature of HSF and CSF, as shown in Equation (3). The relationship of the heat transfer rate between HSF and CSF should satisfy Equation (4) for the steady state of the heat exchanger. The right boundary of CV i and the left boundary of CV i+1 are in the same position in the actual heat exchanger. Therefore, the thermophysical parameters of the nodes on the boundary should be of the same values, as shown in Equation (5) and (6). It is worth noting that the linear interpolation adopted in Equation (1), (2) and (3) may be inappropriate when using relatively small number of FVCVs to approximate the large heat exchanger.

$$\chi_i^{h,c} = \frac{\chi_i^{h,i} + \chi_i^{h,o}}{2} \tag{1}$$

$$\chi_i^{c,c} = \frac{\chi_i^{c,i} + \chi_i^{c,o}}{2} \tag{2}$$

$$T_i^{w} = \frac{T_i^{h,c} + T_i^{c,c}}{2} \tag{3}$$

$$\dot{Q}_i^{h} = \dot{Q}_i^{c} \tag{4}$$

$$\chi_{i+1}^{h,o} = \chi_i^{h,i} \tag{5}$$

$$\chi_{i+1}^{c,i} = \chi_i^{c,o} \tag{6}$$

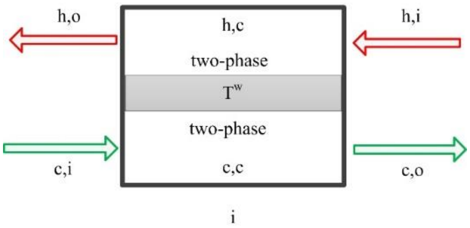

Fig. 3 Single CV

The outlet specific enthalpy of HSF and CSF can be calculated if the inlet parameters of fluids and the heat transfer rate of the CV $\dot{Q}$ are known, as shown in Equation (7) and (8). The other thermophysical parameters of the fluids of the CV can be updated using the function provided by the open source thermal physical property library CoolProp [19] with p and h as the input parameters. The wall temperature of the CV is a key parameter for the calculation of the convective heat transfer coefficients. Thus, if we know the wall temperature of the CV, the convective heat transfer coefficients of HSF and CSF can be calculated as shown in section 2.6 respectively. Furthermore, the heat transfer area of HSF and CSF are shown in Equation (9) and (10) respectively.

$$h_i^{h,o} = h_i^{h,i} - \frac{\dot{Q}_i^{h}}{\dot{m}_i^{h}} \tag{7}$$

$$h_i^{c,o} = h_i^{c,i} + \frac{\dot{Q}_i^{c}}{\dot{m}_i^{c}} \tag{8}$$

$$A_i^{h} = \frac{\dot{Q}_i^{h}}{\alpha_i^{h} \cdot \left(T_i^{h,c} - T_i^{w}\right)} \tag{9}$$

$$A_i^{c} = \frac{Q_i^{c}}{\alpha_i^{c} \cdot \left(T_i^{w} - T_i^{c,c}\right)} \tag{10}$$

2.2. Geometrical of the heat exchanger

The geometrical parameters are crucial to ensure the rest of the algorithm can be correctly executed. The geometrical parameters of plate heat exchanger that can be obtained from technical manual provided by the manufacturer are shown in Fig. 4.

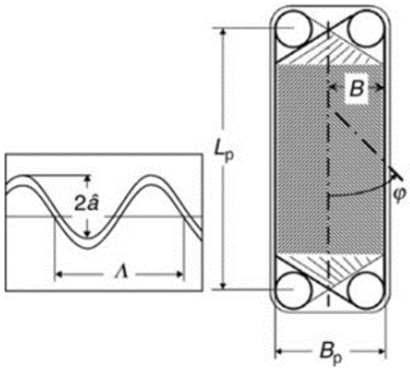

Fig. 4 Main geometrical parameters of single plate appear in plate heat exchanger

With these given parameters, the other important parameters, such as heat transfer area, hydraulic diameters and so on, can be calculated by the method reported in the literature [3]. The detailed description of the calculation procedures is given in Appendix A.

2.3. Initial FVCVs boundary values

The mesh of the FVCVs for a counter-flow heat exchanger divided by FVM is shown in Fig. 5. As can be seen in Fig. 5, the CSF flows from CV 0 to CV m-1, and the HSF flows from CV m-1 to CV 0. The energy of the HSF is transferred to the CSF through the wall between the two fluids, resulting in the temperature decrease and increase of HSF and CSF along with the flow direction. The boundary values of the heat exchanger, such as HSF and CSF outlet parameters, are the basis for starting the iteration processes of FVM. However, these boundary values are unknown parameters for solving and cannot be obtained in advance. Therefore, empirical values are given instead. The empirical values of the inlet and outlet specific enthalpy of HSF and CSF are generated by the linear interpolation of the boundary values of the heat exchanger, as shown in Equation (11) and (12), respectively. When the boundary values of the FVCVs are known, the other parameters needed to start the FVM iteration process can be calculated using Equation (1), (2) and (3), respectively.

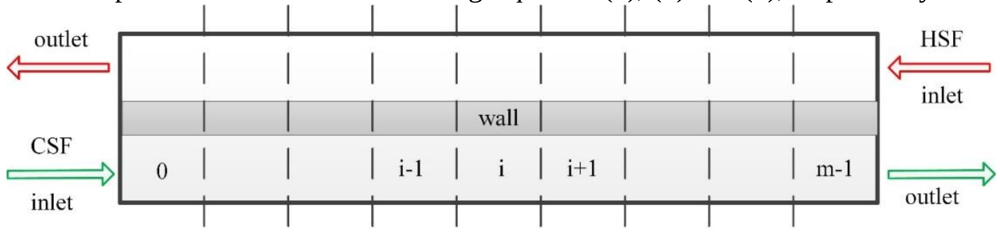

Fig. 5 Mesh of heat exchanger

$$\begin{cases} h_i^{h,o} = h^{h,o} + i \cdot \dfrac{h^{h,i} - h^{h,o}}{n} \\ h_i^{h,i} = h^{h,o} + (i+1) \cdot \dfrac{h^{h,i} - h^{h,o}}{n} \end{cases} \tag{11}$$

$$\begin{cases} h_i^{c,i} = h^{c,i} + i \cdot \dfrac{h^{c,o} - h^{c,i}}{n} \\ h_i^{c,o} = h^{c,i} + (i+1) \cdot \dfrac{h^{c,o} - h^{c,i}}{n} \end{cases} \tag{12}$$

2.4. MBM-based FVCV solving procedures

After the procedures shown in section 2.3, all of the FVCVs have the initial boundary values. However, Equation (4) may not be satisfied by the FVCVs since the enthalpy of HSF and CSF is generated by linear approximation. Therefore, energy balance procedures must be taken to ensure FVCVs satisfy the Equation (4). In addition, fluid phase transition may occur in any FVCV, making the energy balance procedures complexer. To solve the problem properly, the MBM is adopted for the energy balance procedures of FVCV. The MBM shown in this paper is very similar to the one shown in the literature [10], except the required heat transfer area calculation procedures. In other words, the LMTD algorithm is replaced by the iteration of the true wall temperature of the MBCV. The flow chart of the MBM is shown in Fig. 6. It can be seen in Fig. 6 that there exists five steps in the MBM. Firstly, the external pinching analysis is to obtain the upper boundary of the input parameters of the Brent method, in other words, the theoretical maximum heat transfer rate of the FVCV. Secondly, FVCVs are divided into MBCVs for processing the phase change. Thirdly, internal pinching analysis is to update the theoretical maximum heat transfer rate of the FVCV to ensure the correct execution of the Brent method. Fourthly, the actual heat transfer rate of the FVCV is obtained using Brent's method [20]. The more detailed description of these procedures is shown in section 2.4.1 to 2.4.6. The range of the input parameter of Brent method $\dot{Q}$ is shown in Equation (13), where $\dot{Q}_{\max}$ is the minimum value of the results of the internal and external pinch analysis of the FVCV. The convergence criteria of the Brent method, which is the heat transfer area ratio of the calculated to the actual, is shown in Equation (14).

$$0 < \dot{Q} < \dot{Q}_{\max} \tag{13}$$

$$\left| r\left(\dot{Q}\right) \right| < \varepsilon \tag{14}$$

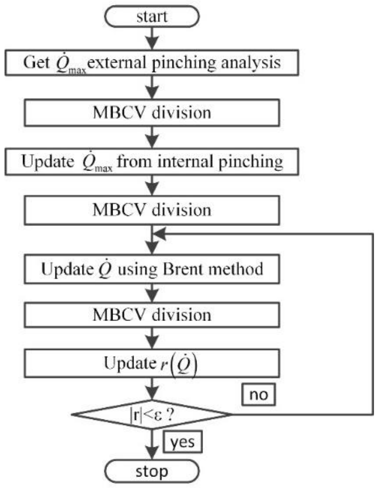

Fig. 6 Flow chart of the MBM based FVCV solving procedures

2.4.1 MBCV division

Due to the heat transfer rate, boundary values and bubble and dew state of HSF and CSF of the FVCV are known parameters, it is very easy to split FVCV into MBCVs where both side fluids are in the definite phase state. Example of the division of the FVCV is shown in Fig. 7. As shown in Fig. 7, two MBCVs are obtained from MBCV division procedures since only bubble node exists in CSF and three MBCVs exists because of the existence of dew node of HSF and CSF. On the condition that both bubble node and dew node exist in HSF and CSF, a maximum of five MBCVs may be obtained from the MBCV division procedures. However, the condition rarely exists in the one FVCV because of the small heat transfer area of FVCV compared to the overall heat exchanger. The group of phase change node and heat balance node constitute the virtual boundary and the FVCV is divided into MBCVs by the virtual boundary in reality. On the condition that HSF or CSF satisfies Equation (15) or Equation (16), then the virtual MBCV boundary exists. The heat balance nodes exist in the virtual MBCV boundary can be updated using Equation (7) and (8) according to HSF and CSF.

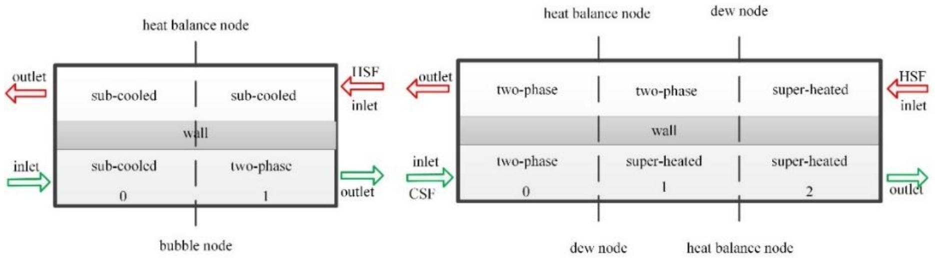

Fig. 7 Example of MBCVs.

$$\begin{cases} p^h < p^{h,crit} \\ h^{h,o} < h^{h,x} < h^{h,i} \end{cases} \tag{15}$$

$$\begin{cases} p^c < p^{c,crit} \\ h^{c,i} < h^{c,x} < h^{c,o} \end{cases} \tag{16}$$

2.4.2 External pinching

The direction of energy transfer, which only goes from high temperature to low temperature, is limited by the second law of thermodynamics. Therefore, the temperature of HSF should always be greater than or at least equal to CSF. As mentioned in section 2.4, the boundary parameters of FVCVs are generated by linear approximation, thus the temperature of HSF and CSF may not satisfy the second law of thermodynamics and the pinching analysis needs to be conducted to eliminate these situations. The external pinching analysis sets the outlet temperature of HSF and CSF to theoretical minimum and maximum value that can be reached, as shown in Equation (17) and (18). With the help of Equation (17) and (18), the heat transfer rate of HSF and CSF can be calculated using Equation (19) and (20). Furthermore, take the results of Equation (17) and (18) as the parameters of Equation (21), the theoretical maximum heat transfer rate of the FVCV can be obtained.

$$T_0^{h,o} = T_0^{c,i} \tag{17}$$

$$T_{m-1}^{c,o} = T_{m-1}^{h,i} \tag{18}$$

$$\dot{Q}_{ext}^h = \dot{m}^h \cdot \left(h_{m-1}^{h,i} - h_0^{h,o} \right) \tag{19}$$

$$\dot{Q}_{ext}^c = \dot{m}^c \cdot \left(h_{m-1}^{c,o} - h_0^{c,i} \right) \tag{20}$$

$$\dot{Q}_{ext} = \min\left(\dot{Q}_{ext}^h, \dot{Q}_{ext}^c \right) \tag{21}$$

2.4.3 Internal pinching

The second law of thermodynamics should not only be satisfied with the boundary temperature of FVCV, but also the boundary temperature of MBCVs. Therefore, the internal pinching analysis, whose purpose is to remove the impossible temperature distribution of the internal MBCV, should be executed. The possible position of internal pinching of HSF and CSF is the phase change point, thus the internal pinching analysis simply resets the temperature of the phase change node and the heat balance node to reasonable values. Bubble point is the reasonable internal pinching point that appears in CSF, as shown in Equation (22). If the internal pinching point of CSF exists, update of the heat transfer rate of CSF is needed, as shown in Equation (23). Similarly, Dew point is the reasonable internal pinching point that appears in HSF, as shown in Equation (24). If the internal pinching point of HSF exists, the heat transfer rate of HSF is needed to be updated using Equation (25).

$$T_i^{h,i} = T_i^{c,bp} \tag{22}$$

$$\dot{Q}_{\mathrm{int}}^{c} = \dot{m}^c \cdot \left(h_i^{c,bp} - h_0^{c,i}\right) + \dot{m}^h \cdot \left(h_{m-1}^{h,i} - h_i^{h,i}\right) \tag{23}$$

$$T_i^{c,o} = T_i^{h,dp} \tag{24}$$

$$\dot{Q}_{\mathrm{int}}^{h} = \dot{m}^c \cdot \left(h_i^{c,o} - h_0^{c,i}\right) + \dot{m}^h \cdot \left(h_{m-1}^{h,i} - h_i^{h,dp}\right) \tag{25}$$

2.4.4 Theoretical maximum heat transfer rate of the FVCV

The theoretical maximum heat transfer rate is an input parameter of Brent's method, as shown in Equation (26). In Equation (26), $\dot{Q}_{ext}$ is defined by Equation (21) and $\dot{Q}_{\mathrm{int}}^{h}$ and $\dot{Q}_{\mathrm{int}}^{c}$ are defined by Equation (23) and (25) respectively.

$$\dot{Q}_{\max} = \min\left(\dot{Q}_{ext}, \dot{Q}_{\mathrm{int}}^{h}, \dot{Q}_{\mathrm{int}}^{c}\right) \tag{26}$$

2.4.5 Required heat transfer area for MBCVs

The updated wall temperature of MBCV can be calculated by Equation (27), the result of the combination of Equation (4), (9) and (10). The unknown parameter R, which is defined as the heat transfer area ratio of HSF to CSF of the heat exchanger, is shown in Equation (28). Note that R is an inherent parameter of the heat exchanger and can be obtained from the geometry parameters of the heat exchanger. One more thing should be noted is the omittance of the thermal resistance of the wall in Equation (27). Afterwards, the iteration of the wall temperature of the MBCV can be started until Equation (29) is satisfied by the MBCV. When the wall temperature of the MBCV is updated, Equation (9) and (10) can be adopted to update the required heat transfer area for HSF and CSF respectively. When the required heat transfer area of MBCVs is updated, a summation process is needed to calculate the required heat transfer area of FVCV, as shown in Equation (30) and (31).

$$T_j^{w,u} = \frac{R \cdot \alpha_j^h \cdot T_j^{h,c} + \alpha_j^c \cdot T_j^{c,c}}{R \cdot \alpha_j^h + \alpha_j^c} \tag{27}$$

$$R = \frac{A^h}{A^c} \tag{28}$$

$$\left|T^w - T^{w,u}\right| < 0.1 \tag{29}$$

$$A_i^{h,r} = \sum_{j=0}^{n-1} A_j^h \tag{30}$$

$$A_i^{c,r} = \sum_{j=0}^{n-1} A_j^c \tag{31}$$

The residual function using in Brent method for the convergence estimate is shown in Equation (32), where the ratio of the hot side required to the actual heat transfer area of the heat exchanger is adopted.

$$r\left(\dot{Q}\right) = 1 - \frac{A_i^{h,r}}{A_i^h} \tag{32}$$

2.5. FVCVs boundary value update procedures

The energy balance of each of the FVCVs is guaranteed by the procedures of Section 2.4. However, Equation (5) or (6) may not be satisfied by the FVCVs, thus the convergence of the heat exchanger is not guaranteed. Therefore, the inlet parameters of HSF and CSF of the FVCVs need to be updated according to Equation (5) and (6). The convergence of the heat exchanger is guaranteed if the outlet enthalpy of HSF and CSF satisfy Equation (33).

$$\begin{cases} \Delta h^{c,o} = \left| h^{c,o} - h^{c,o,u} \right| < \varepsilon \\ \Delta h^{h,o} = \left| h^{h,o} - h^{h,o,u} \right| < \varepsilon \end{cases} \tag{33}$$

2.6. Convective heat transfer coefficient of the plate heat exchanger

The single phase heat transfer coefficient correlations of Martin [3] are adopted in this paper as shown in Equation (34). The two phase heat transfer coefficient correlations of Huang [21] are adopted in this paper as shown in Equation (35). The details of these correlations are further reported in Appendix B.1 and B.2 for simplicity.

$$Nu_{sp} = \frac{\alpha_{sp} D_h}{k} = c_q \, \mathrm{Pr}^{(1/3)} \left(\eta / \eta_w\right)^{(1/6)} \left[2Hg \sin 2\varphi\right]^q \tag{34}$$

$$Nu_{tp} = \frac{\alpha_{tp} D_h}{k_l} = 1.87 \times 10^{-3} \left[\frac{q'' d_0}{k_l T_{sat}}\right]^{0.56} \left[\frac{\Delta h_{fg} d_0}{\gamma_l^2}\right]^{0.31} \mathrm{Pr}^{0.33} \tag{35}$$

3. Validation

In order to evaluate the accuracy of the heat exchanger model reported in this paper, the 11 experimental steady state operating conditions shown in Table C.1 of the plate heat exchanger are adopted to validate the heat exchanger model.

3.1. Geometry and fluids inlet parameters of the plate heat exchanger

The geometry parameters of the heat exchanger are shown in Table 1 and the application range of T66 and R245fa is shown in Table 2. The inlet parameters of HSF and CSF of the plate heat exchanger which are obtained from Table A.2 of the literature [11] are shown in Table C.1 for the purpose of simplicity.

Table 1 Geometry parameters of the plate heat exchanger

Parameter	unit	Value
Model	-	SWEP B200T SC-M
N_p	-	150
B_p	m	0.243
L_p	m	0.525
â	m	0.94E-3
Λ	m	0.3E-3
Temperature range	℃	-196~225
Maximal pressures	MPa	4.5 at 135℃ and 3.6 at 225℃
Material	-	Stainless steel
Weight	kg	69.8

Table 2 Application range of fluids in heat exchangers

Parameter	T_{min}(℃)	T_{max}(℃)	p_{max}(MPa)	d_{max}(kg/m^3)	p_{crit}(MPa)	T_{crit}(℃)
T66	-7	345	-	-	-	-

R245fa	-102.1	166.85	200.0	1648.8	3.651	154.01

3.2. Effect of the FV mesh size on the heat transfer rate

An analysis of the FV mesh size effect on the heat transfer rate is carried out and the results are shown in Fig. 8. It can be seen from Fig. 8 that the heat transfer rate of the 11 cases of the plate heat exchanger is declining along with the FV mesh size increase. However, when the FV mesh size is larger than 10, the variation of the heat transfer rate is very little among the 11 cases. Therefore, the FV mesh size is set to 10 in the following sections of the paper.

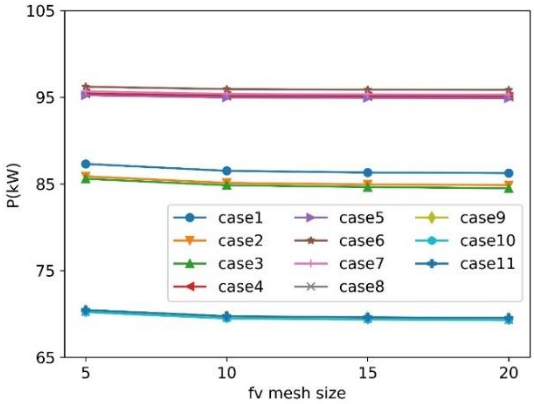

Fig. 8 Effect of the FV mesh size on the heat transfer rate

3.3. Heat transfer rate validation of the plate heat exchanger

In this paper, the heat transfer rate of the plate heat exchanger is adopted to validate the accuracy of the heat exchanger model and the results are shown in Fig. 9. Note that the x and y axis are the simulation and experimental heat transfer rate of the plate heat exchanger respectively. As can be seen from Fig. 9, the heat transfer rate deviates less than ±4% from the equal line. Therefore, the model proposed in this paper is able to predict the heat exchanger performances with enough accuracy.

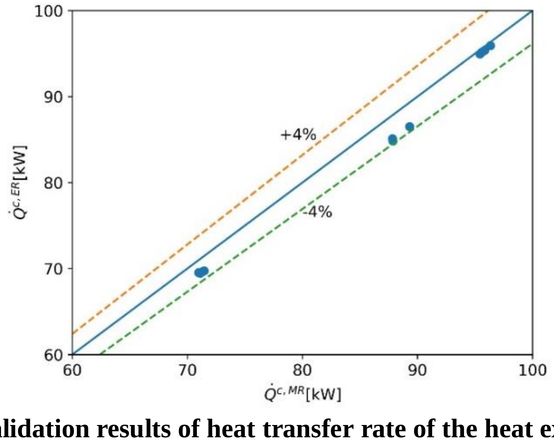

Fig. 9 Validation results of heat transfer rate of the heat exchanger

4. Case study

For the purpose of deeply understanding the computing procedures of the novel coupling discretization method, the detailed simulation results of case 1 and brief discussions are illustrated in the following parts of the paper. The similar results can be obtained in the rest of the cases, thus not shown in this paper anymore.

4.1. Simulation results

The temperature and quality distribution of FVCVs and MBCVs are shown in Fig. 10. The temperature and quality distribution of FVCVs are shown in the lower sub-figure of Fig. 10, while the temperature and quality distribution of the phase change FVCV are more detailed shown in the upper sub-figure of Fig. 10. As can be seen from Fig. 10, CSF phase change happens in FVCV 3 and 8 during the heat transfer process of HSF and CSF, in which the phase state of CSF varies from sub-cooled to two-phase in FVCV 3 and from two-phase to super-heated in FVCV 8. Since no phase change occurs in the other FVCVs, only one MBCV exists in the MBM based on FVCV solving procedures. In this condition, the MBCV will be equivalent to FVCV and thus not repeated shown in Fig. 10. The temperature of HSF and CSF in the FVCVs has a nonlinear distribution due to the different heat transfer coefficient and temperature difference of the FVCV. The temperature slope of CSF in sub-cooled region is larger than that of the super-heated region because of the large temperature difference of CSF in sub-cooled region. On the contrary, the slope of HSF temperature has been slightly smoothed since the large specific heat of HSF. At last, the pinch point of case 1 appears on the bubble point of CSF.

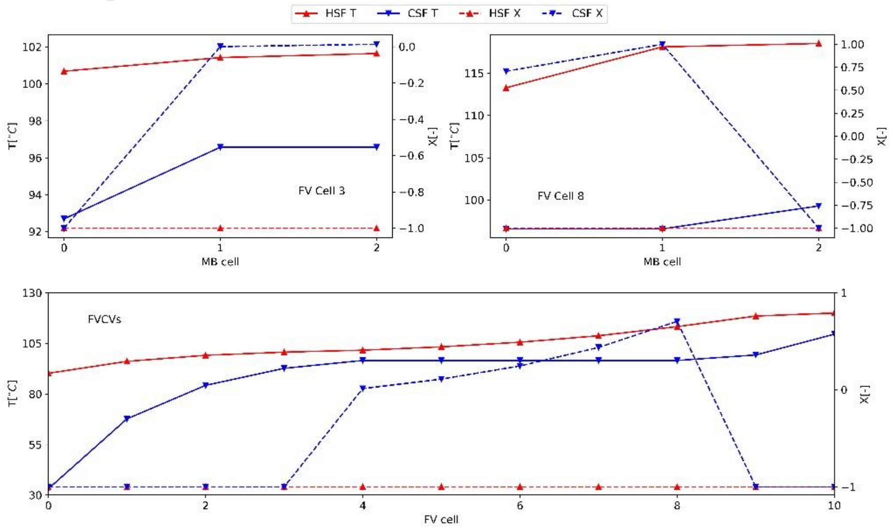

Fig. 10 Temperature and quality distribution of FVCVs and MBCVs

The convective heat transfer coefficient distribution of FVCVs is shown in Fig. 11. It can be seen from Fig. 11 that the convective heat transfer coefficient of HSF is almost the same in all of the FVCVs, with only slight change occurring at FVCV 0, 8b and 9. However, the convective heat transfer coefficient of CSF changes significantly in the phase change FVCV and the two-phase FVCV. The change of the former is mainly due to the phase change in FVCV x, so that the FVCV x is represented as MBCV xa and xb in Fig. 11, where MBCV xa and xb represent the sub-liquid part and two-phase part of the FVCV 3 respectively. Nevertheless, the change of the latter is mainly due to the bubbles occurring in the two-phase region and the evaporation heat transfer. It can be obviously seen from Fig. 11 that the convective heat transfer coefficient of CSF in two-phase region is significantly larger than that of the single phase region due to the strong disturbance caused by the formation and detachment of bubbles.

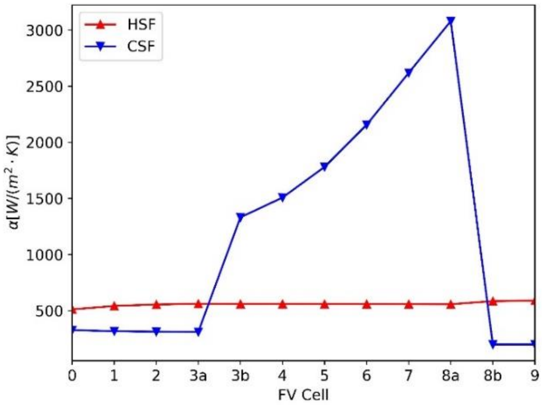

Fig. 11 Convective heat transfer coefficient distribution of FVCVs and MBCVs

The wall temperature distribution of FVCVs is shown in Fig. 12. The wall temperature rises sharply when CSF flows in sub-liquid region and super-heated region because of the relatively large heat transfer temperature difference between HSF and CSF. However, the wall temperature gradually levels out along with CSF beginning to evaporate due to the decrease of the heat transfer temperature difference between HSF and CSF. Moreover, only slight rise of the wall temperature is observed when CSF flows in the two-phase region due to relatively small change of the temperature of HSF.

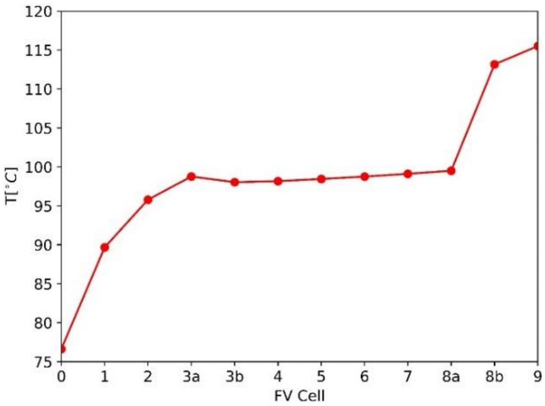

Fig. 12 Wall temperature distribution of FVCVs and MBCVs

The heat transfer area distribution of the FVCVs is shown in Fig. 13. As can be seen from Fig. 11, the heat transfer area of each FVCV is equal under the precondition of the FVM. Note that the heat transfer area of FVCV 3 and 8 is split into two parts by the MBM based on FVCV solving procedures and is actually equal to the sum of the two parts. The heat transfer area of FVCV 3a and 3b represents the sub-liquid and two-phase part of FVCV 3 respectively. Accordingly, the heat transfer area of FVCV 8a and 8b represents the two-phase and super-heated part of FVCV 8 respectively.

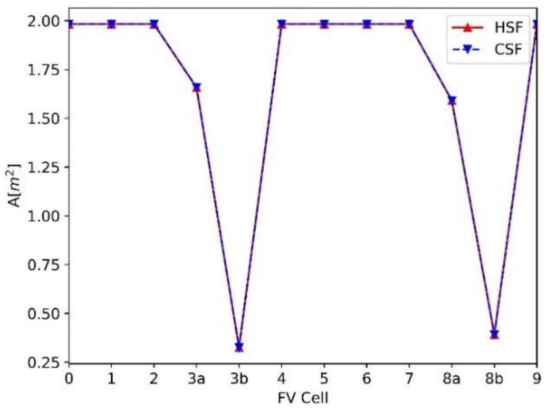

Fig. 13 Heat transfer area distribution of FVCVs and MBCVs

5. Conclusion

The performance of the ORC evaporator and condenser significantly affects cycle efficiency. Therefore, modeling of heat exchangers is important for the development of the ORC system simulation tools. In this paper, we proposed a novel coupling discretization method for modeling heat exchangers with fluid phase change. The proposed algorithm is proved to be effective to the ORC heat exchangers solving and can be easily integrated with the ORC system simulation tools. In addition, the accuracy of the algorithm is verified by the 11 steady state experimental operating conditions and the results show that the algorithm can meet the engineering requirements. The detailed results of case 1 are shown in section 6 for the purpose of deeply understanding the computing procedures of the novel coupling discretization method. Our future work will be focused on the integration of the algorithm with the ORC system simulation tools and verify the performance of the ORC system simulation tools.

Appendix A. Geometry parameters of plate heat exchanger

The area of one plate of the plate heat exchanger is shown in Equation (A.1).

$$A_p = \Phi \cdot A_0 \tag{A.36}$$

Where A0 is the plane surface area which is shown in Equation (A.2) and Φ is calculated in Equation (A.3). The unknown parameter X in Equation (A.3) is defined in Equation (A.4). The hydraulic diameter of the plate heat exchanger is defined in Equation (A.5).

$$A_0 \approx B_p L_p \tag{A.37}$$

$$\Phi(X) \approx \frac{1}{6}\left(1+\sqrt{1+X^2}+4\sqrt{1+X^2/2}\right) \tag{A.38}$$

$$X = \frac{2\pi\hat{a}}{\Lambda} \tag{A.39}$$

$$D_h = \frac{4\hat{a}}{\Phi} \tag{A.40}$$

The total heat transfer area of the plate heat exchanger can be simply calculated in Equation (A.6).

$$A^h = A^c = A_p \cdot \left(N_p - 2\right) \tag{A.41}$$

The hot side and cold side total cross section area of the gap of the two plates is calculated in Equation (A.7) and (A.8) respectively.

$$A_{gap}^h = 2 \cdot \hat{a} \cdot B_p \cdot N_{gap}^h \tag{A.42}$$

$$A_{gap}^c = 2 \cdot \hat{a} \cdot B_p \cdot N_{gap}^c \tag{A.43}$$

Appendix B. Single phase and two-phase evaporation heat transfer coefficient of plate heat exchanger

B.1. Single phase heat transfer

For the single phase heat transfer in plate heat exchanger, the Nusselt number shown in Equation (A.9) is adopted in this paper. The value of the constants cq and q is set to 0.122 and 0.374 respectively. The unknown parameter Hg is calculated in Equation (A.10). In Equation (A.10), Re and ζ are obtained from Equation (A.11) and (A.13) respectively. The mass flux G in Equation (A.12) is obtained from Equation (A.12) and the unknown parameters ζ0 and ζ1 are acquired by combining

Equation (A.14) or (A.15) with (A.16). Note that Equation (A.14) is accepted if Re < 2000, otherwise Equation (A.15) will be accepted.

$$Nu_{sp} = \frac{\alpha_{sp} D_h}{k} = c_q \, \mathrm{Pr}^{(1/3)} \left(\eta/\eta_w\right)^{(1/6)} \left[2Hg \sin 2\varphi\right]^q \tag{A.44}$$

$$Hg = \frac{\mathrm{Re}^2 \zeta}{2} \tag{A.45}$$

$$\mathrm{Re} = \frac{G \cdot D_h}{\mu} \tag{A.46}$$

$$G = \frac{\dot{m}}{A_{gap}} \tag{A.47}$$

$$\frac{1}{\sqrt{\zeta}} = \frac{\cos\varphi}{\sqrt{b\tan\varphi + c\sin\varphi + \zeta_0/\cos\varphi}} + \frac{1-\cos\varphi}{\sqrt{\zeta_1}} \tag{A.48}$$

$$\begin{cases} \zeta_0 = \dfrac{64}{\mathrm{Re}} \\ \zeta_{1,0} = \dfrac{597}{\mathrm{Re}} + 3.85 \end{cases} \tag{A.49}$$

$$\begin{cases} \zeta_0 = \dfrac{1}{(1.8\ln(\mathrm{Re}) - 1.5)^2} \\ \zeta_{1,0} = \dfrac{39}{\mathrm{Re}^{0.289}} \end{cases} \tag{A.50}$$

$$\zeta_1 = \mathrm{a} \cdot \zeta_{1,0} \tag{A.51}$$

B.2. Two-phase evaporation heat transfer

For the two phase evaporation heat transfer in plate heat exchanger, the Nusselt number shown in Equation (A.17) is adopted in this paper. In Equation (A.17), Tsat is the saturation temperature of the fluid, d0 is the bubble departure diameter as shown in Equation (A.18) and γ is the thermal diffusivity as shown in Equation (A.19).

$$Nu_{tp} = \frac{\alpha_{tp} D_h}{k_l} = 1.87\times10^{-3} \left[\frac{q^{"} d_0}{k_l T_{sat}}\right]^{0.56} \left[\frac{\Delta h_{fg} d_0}{\gamma_l^2}\right]^{0.31} \mathrm{Pr}^{0.33} \tag{A.52}$$

$$d_0 = 0.0146 \cdot \theta \cdot \left[\frac{2\sigma}{g\left(\rho_l - \rho_v\right)}\right]^{0.5} \tag{A.53}$$

$$\gamma_l = \frac{k}{\rho c_p} \tag{A.54}$$

Appendix C. Inlet and outlet parameters of fluids of the 11 steady state operating conditions

(see Table C.1)

Table C.1 Inlet and outlet parameters of fluids of the 11 steady state operating conditions

Parameter	1	2	3	4	5	6	7	8	9	10	11
HSF	T66										
$\dot{m}^h$	1.568	1.565	1.566	3.005	3.003	3.003	3.005	1.494	1.496	1.505	1.504
$T^{h,i}$	120.0	120.0	120.0	119.9	119.9	120.0	119.9	109.9	110.0	109.9	110.0
$H^{h,i}$	174.1	174.1	174.1	173.9	173.9	174.1	173.9	155.0	155.2	155.0	155.2
$p^{h,i}$	1.0	1.0	1.0	1.0	1.0	1.0	1.0	1.0	1.0	1.0	1.0
$X^{h,i}$	-1	-1	-1	-1	-1	-1	-1	-1	-1	-1	-1
$T^{h,o,ER}$	89.7	90.3	90.3	103.3	103.2	103.1	103.1	83.1	83.1	83.0	83.3
$H^{h,o,ER}$	117.9	118.9	118.9	142.7	142.5	142.4	142.4	106.1	106.1	105.9	106.5
$T^{h,o,MR}$	90.2	90.7	90.8	102.9	102.9	102.9	102.9	84.4	84.4	84.6	84.6
$H^{h,o,MR}$	118.8	119.6	119.8	142.1	142.2	142.1	142.0	108.3	108.5	108.7	108.7

$p^{h,o}$	1.0	1.0	1.0	1.0	1.0	1.0	1.0	1.0	1.0	1.0	1.0
$X^{h,o}$	-1	-1	-1	-1	-1	-1	-1	-1	-1	-1	-1
CSF	R245fa										
$\dot{m}^{c}$	0.352	0.350	0.353	0.383	0.383	0.387	0.385	0.290	0.292	0.291	0.292
$T^{c,i}$	33.5	35.9	36.5	38.1	38.5	38.5	38.5	35.7	35.7	35.7	35.5
$H^{c,i}$	244.5	247.7	248.5	250.7	251.3	251.3	251.3	247.4	247.4	247.4	247.2
$p^{c,i}$	1.171	1.167	1.178	1.266	1.266	1.270	1.271	0.972	0.972	0.973	0.975
$X^{c,i}$	-1	-1	-1	-1	-1	-1	-1	-1	-1	-1	-1
$T^{c,o,ER}$	116.3	116.6	115.7	119.4	119.5	119.4	119.4	108.1	107.8	107.8	107.9
$H^{c,o,ER}$	498.3	498.7	497.4	500.3	500.4	500.2	500.2	492.2	491.8	491.8	491.9
$T^{c,o,MR}$	109.6	110.4	108.9	118.9	118.9	118.9	118.8	102.7	103.1	103.2	103.1
$H^{c,o,MR}$	489.8	490.9	488.9	499.2	499.2	499.1	499.0	485.5	486.0	486.2	485.9
$p^{c,o}$	1.171	1.167	1.178	1.266	1.266	1.270	1.271	0.972	0.972	0.973	0.975
$X^{c,o}$	-1	-1	-1	-1	-1	-1	-1	-1	-1	-1	-1

Nomenclature

â - amplitude of the corrugation (m)
A - heat transfer area (m^2)
A_0 - plane projection of the plate surface (m^2)
A_p - actual plate surface (m^2)
B - width of the corrugation pattern (m)
Bp - plate width (m)
c_q - factor in modified Lévêque analogy (1)
d_0 - bubble departure diameter (m)
D_h - hydraulic diameter (m)
h - Enthalpy (kJ/kg)
Hg - Hagen number (1)
k - thermal conductivity ($W/(m^2 \cdot K)$)
L - length between two crossing points (m)
L_p - plate length (m)
m - total number of FVCVs
$\dot{m}$ - mass flow rate (kg s-1)
N_p - number of the plate (1)
Nu - nusselt number (1)
p - pressure (Pa)
Pr - prandtl number (1)
q - exponent in modified Lévêque analogy (1)
q'' - heat flux ($W \cdot m^2$)
$\dot{Q}$ - heat transfer rate (kW)
Re - Reynolds number
s - Entropy ($kJ/(kg \cdot K)$)
T - Temperature (°C)
X - quality (1) or wave number (1)

Acronyms

CV - Control Volume
CSF - Cold Side Fluid
ER - Experimental Results
FVM - Finite Volume Method
FVCV - Finite Volume Control Volume
HSF - Hot Side Fluid
LMTD - Log Mean Temperature Difference
MR - Modeling Results
MBM - Moving Boundary Method
MBCV - Moving Boundary Control Volume
NTU - Number of Transfer Units
ORC - Organic Rankine Cycle
R - heat transfer area ratio
WHR - Waste Heat Recovery

Greek symbols

α - convective heat transfer coefficient ($W/(m^2 \cdot K)$)
γ - thermal diffusivity, m^2/s
ε - effectiveness of heat exchanger or residual
η - viscosity ($Pa \cdot s$)
Λ - wavelength (m)
ρ - density (kg/m^3)
φ - inclination angle of the corrugation
Φ - surface enhancement factor (1)
χ - fluid state parameter, which stands for T, p, H, S, or X

Subscripts

ext - external
fg - latent heat of evaporation
i - FVCV index
int - internal
l - saturation liquid
min - minimum
sat - saturation
sp - single phase
tp - two phase
w - at wall temperature

max - maximum	
Superscripts	
bp - bubble point	o - outlet
c - cold, center, calculate	r - required
crit - critical point	s - shell
dp - dew point	t - tube
g - geometry	u - update
h - hot	w - wall
i - inlet	x - bp or dp
id - ideal	

References

[1] Sprouse C., *et al.*, Review of Organic Rankine Cycles for internal combustion engine exhaust waste heat recovery, *Applied Thermal Engineering*, 51 (2013), pp. 711–722

[2] Woolley E., *et al.*, Industrial waste heat recovery: A systematic approach, Sustain. *Energy Technol. Assessments*, 29 (2018), pp. 50–59

[3] VDI-GVC, VDI Heat Atlas, Berlin, Heidelberg, 2010.

[4] Qiao H., *et al.*, A new model for plate heat exchangers with generalized flow configurations and phase change, *Int. J. Refrig*, 36 (2013), pp. 622–632

[5] Patiño J., *et al.*, A comparative analysis of a CO_2 evaporator model using experimental heat transfer correlations and a flow pattern map, *Int. J. Heat Mass Transf*, 71 (2014), pp. 361–375

[6] Chowdhury J. I., *et al.*, Modelling of evaporator in waste heat recovery system using finite volume method and fuzzy technique, *Energies*, 8 (2015), pp. 14078–14097

[7] Yohanis Y.G., *et al.*, A simplified method of calculating heat flow through a two-phase heat exchanger, *Appl. Therm*. *Eng*, 25 (2005), pp. 2321–2329

[8] Zegenhagen M.T., *et al.*, Simple models for the heat exchange from exhaust gas to super- and sub-critical refrigerant R134a at high temperature differences, *Appl. Therm. Eng*, 89 (2015), pp. 990–1000

[9] Gullapalli V.S., *et al.*, Modeling of brazed plate heat exchangers for ORC systems, *Energy Procedia*, 129 (2017), pp. 443–450

[10] Bell I. H., *et al.*, A generalized moving-boundary algorithm to predict the heat transfer rate of counterflow heat exchangers for any phase configuration, *Appl. Therm. Eng*, 79 (2015), pp. 192–201

[11] Lecompte S., *et al.*, Experimental results of a small-scale organic Rankine cycle: Steady state identification and application to off-design model validation, *Appl. Energy*, 226 (2018), pp. 82–106

[12] Sarfraz O., *et al.*, Discrete modeling of fin-and-tube heat exchangers with cross-fin conduction functionality, *Int. J. Refrig*, 104 (2019), pp. 270–281

[13] Taler D., *et al.*, Mathematical modeling and control of plate fin and tube heat exchangers, *Energy Convers. Manag*, 96 (2015), pp. 452–462

[14] Huang R., *et al.*, Comparison of approximation-assisted heat exchanger models for steady-state simulation of vapor compression system, *Appl. Therm. Eng*, 166 (2020), pp. 114691

[15] Bone V., *et al.*, Methodology to develop off-design models of heat exchangers with non-ideal fluids, *Appl. Therm. Eng*, 145 (2018), pp. 716–734

[16] Jahn I. H. J., *et al.*, Code for the Design and Evaluation of Heat Exchangers for Complex Fluids

With Contributions from: Samuel Roubin, Report No. 04, The University of Queensland, Queensland, Australia, 2017

[17] Hagen B. A. L., *et al.*, A novel methodology for Rankine cycle analysis with generic heat exchanger models, *Appl. Therm. Eng*, 165 (2020), pp. 114566

[18] Chu Z., *et al.*, Moving-boundary and finite volume coupling algorithm for heat exchanger with fluid phase change, *Int. J. Heat Mass Transf*, 131 (2019), pp. 313–328

[19] Bell, I. H., *et al.*, Pure and Pseudo-Pure Fluid Thermophysical Property Evaluation and the Open-Source Thermophysical Property Library Coolprop, *Industrial and Engineering Chemistry Research*, 53 (2014), pp. 2498-2508

[20] Brent R, Algorithms for Minimization Without Derivatives, Prentice-Hall, 1973

[21] Huang J., *et al.*, Heat transfer and pressure drop in plate heat exchanger refrigerant evaporators, *Int. J. Refrig*, 35 (2012), pp. 325–335

Paper submitted: 09 September 2022
Paper revised: 09 January 2023
Paper accepted: 13 January 2023